



01 Jun 2007

Magnetic Equivalent Circuit Modeling of Induction Motors

S. D. Sudhoff

Brian T. Kuhn

Keith Corzine

Missouri University of Science and Technology

Brian T. Branecky

Follow this and additional works at: https://scholarsmine.mst.edu/ele_comeng_facwork

 Part of the [Electrical and Computer Engineering Commons](#)

Recommended Citation

S. D. Sudhoff et al., "Magnetic Equivalent Circuit Modeling of Induction Motors," *IEEE Transactions on Energy Conversion*, Institute of Electrical and Electronics Engineers (IEEE), Jun 2007.

The definitive version is available at <https://doi.org/10.1109/TEC.2006.875471>

This Article - Journal is brought to you for free and open access by Scholars' Mine. It has been accepted for inclusion in Electrical and Computer Engineering Faculty Research & Creative Works by an authorized administrator of Scholars' Mine. This work is protected by U. S. Copyright Law. Unauthorized use including reproduction for redistribution requires the permission of the copyright holder. For more information, please contact scholarsmine@mst.edu.

Magnetic Equivalent Circuit Modeling of Induction Motors

Scott D. Sudhoff, *Senior Member, IEEE*, Brian T. Kuhn, *Member, IEEE*, Keith A. Corzine, *Member, IEEE*,
and Brian T. Branecky

Abstract—Finite element models are invaluable for determining expected machine performance. However, finite element analysis can be computationally intense; particularly if a large numbers of studies or high bandwidth studies are required. One method to avoid this difficulty is to extract machine parameters from the finite element model and use the parameters in lumped parameter models. While often useful, such an approach does not represent space harmonics or asymmetries in the motor. A methodology for constructing a state-variable model, based on a magnetic equivalent circuit of the motor is described herein. In addition, the parameters for this model are based solely on geometrical data. This approach is an excellent compromise between the speed of lumped parameter models and the ability of finite element methods to capture spatial effects. Experimental validation of the model is provided.

Index Terms—Geometry-based modeling, induction machine modeling, magnetic equivalent circuit (MEC), space harmonics.

I. INTRODUCTION

Finite element analysis (FEA) is a common method of studying spatial harmonics in electric machinery. This analysis can yield excellent accuracy, but is computationally intense. Other analysis approaches that include spatial effects are magnetically coupled circuit modeling [1], [2] and magnetic equivalent circuit (MEC) modeling [3]–[8]. This latter approach has the advantage of a close association with the physical field distributions in the machine. It has been applied to a variety of machines including induction machines [3]–[6], synchronous machines [7], and switched reluctance machines [8].

The MEC approach has the advantage that it includes spatial dependencies as in the case of FEA, but is computationally less intense, thereby allowing it to be used in higher bandwidth studies in which the interaction of power converter and machine is important, or in situations where a large number of studies are required (for example, population-based automated design techniques). Simply put, MEC modeling can provide a compromise between finite element and qd -type models.

Manuscript received September 3, 2003; revised January 10, 2006. This work was supported in part by A. O. Smith Corporation and in part by the Office of Naval Research through the ESRDC. Paper no. TEC-00228-2003.

S. D. Sudhoff is with the Department of Electrical and Computer Engineering, Purdue University, West Lafayette, IN 47907 USA (e-mail: sudhoff@ece.purdue.edu).

B. T. Kuhn is with SmartSpark Energy Systems, Champaign, IL 61820 USA (e-mail: b.kuhn@smartsparkenergy.com).

K. A. Corzine is with the Department of Electrical and Computer Engineering, University of Missouri-Rolla, Rolla, MO 65409 USA (e-mail: corzine@umr.edu).

B. T. Branecky is with A. O. Smith Corporation, Milwaukee, WI 53224 USA (e-mail: bbranecky@aosmith.com).

Digital Object Identifier 10.1109/TEC.2006.875471

In this paper, the MEC approach to modeling the induction machine is examined in detail. A model is developed, which is based solely on geometrical data, material parameters, and winding distributions. The model takes into account local saturation of individual stator and rotor teeth as well as the back-iron sections of the machine. Also, it takes rotor skewing, stator and rotor tooth effects, space harmonics in the stator windings and rotor bars, and end ring flux components into account. It is valid for asymmetrical excitation, broken end ring, and broken rotor bar conditions. One limitation of the proposed model is that the accuracy during transient conditions is limited because it does not include distributed circuit effects in the rotor conductors. An additional factor that may limit performance during transients is that stator end ring leakage inductance has not been included.

Of the prior work in the MEC area, the approach herein is perhaps most similar to [3] and [4]. However, this work features a more integrated treatment of the flux linkage and node potential equations, and utilizes a qd framework that is beneficial in treating leakage inductance. The use of a qd framework in order to simplify the calculation of the leakage inductance is also used in [5]; however, that model is restricted to the magnetically linear condition. Unlike [6], this work sets forth expressions for permeance in terms of geometrical data rather than relying on a secondary FEA analysis. Finally, this paper sets forth a much more detailed algorithm to calculate the permeances than [3]–[6]. As an aside, it has been recently shown [9] that a bar-by-bar type representation can be reduced to a system with only four states; however, this is restricted to symmetrical and magnetically linear conditions.

II. NOTATION AND OPERATORS

Throughout this work, scalar quantities will be designated with italics while matrix/vector quantities will appear in boldface. Two variables, i and j , will denote matrix/vector indexes when used in a subscript. In this context, i refers to stator quantities and takes on values $[1, \dots, N_{ss}]$ where N_{ss} is the number of stator slots. The index j refers to rotor quantities and will take on values $[1, \dots, N_{rs}]$ where N_{rs} is the number of rotor slots. Integer operations on these indexes are ring-mapped back to the set. For example, if operating on the stator set index with $N_{ss} = 12$, then $12 + 1$ maps to 1 and $1 - 1$ maps to 12.

This paper will make use of an element-by-element vector multiply. Given three vectors $x, y, z \in \mathbb{R}^N$ where \mathbb{R} denotes the set of real numbers and N is in the set of natural numbers, the element-by-element multiply given by

$$z_k = x_k y_k \quad k \in [1, \dots, N] \quad (1)$$

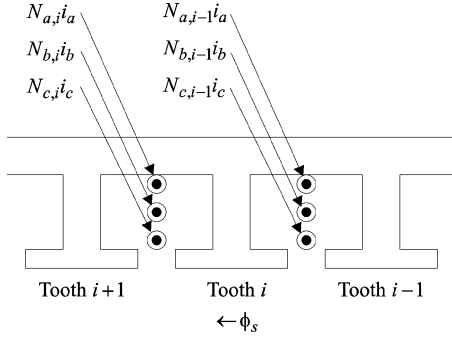


Fig. 1. Stator geometry.

will be denoted

$$z = x \circ y. \quad (2)$$

The \circ operator is commutative and associative and its implied order of operation is higher than multiplication.

Throughout this paper, Heaviside notation p is used for the time derivative operator, i.e.,

$$p = \frac{d}{dt}. \quad (3)$$

III. MODEL STRUCTURE

A. Stator Definitions

The machine considered herein is assumed to possess a three-phase stator winding. Stator variables are denoted in a form f_x where “ f ” may be a voltage v , current i (positive into the machine), or flux linkage λ , and “ x ” may be “ a ,” “ b ,” or “ c .” Stator quantities are also represented as vectors of the form

$$\mathbf{f}_{abc} = [f_a \ f_b \ f_c]^T \quad (4)$$

where the superscript T denotes the transpose operator. In terms of abc variables, the stator voltages, currents, and flux linkages are related by Ohm’s and Faraday’s laws; in particular, the stator voltage equation may be expressed

$$\mathbf{v}_{abc} = r_s \mathbf{i}_{abc} + p \boldsymbol{\lambda}_{abc} \quad (5)$$

where r_s is the stator winding resistance.

The stator geometry is depicted in Fig. 1. The stator slots are numbered $1-N_{ss}$. The i th slot contains $N_{a,i}$ turns of the a -phase winding, $N_{b,i}$ turns of the b -phase winding, and $N_{c,i}$ turns of the c -phase winding, where positive turns are out of the page. The turns vector $\mathbf{N}_{abc,i}$ is defined as

$$\mathbf{N}_{abc,i} = [N_{a,i} \ N_{b,i} \ N_{c,i}]^T. \quad (6)$$

The number of spans describes the number of times each phase winding links the radial field density at a position ϕ_s along the stator, where ϕ_s is referenced from the center of stator tooth 1 and measured in the counterclockwise direction as viewed from the front of the machine.

The winding function [10] is a measure of the number of times that a given winding set links the flux density at a position ϕ_s . Taking the positive direction of flux density to be from the

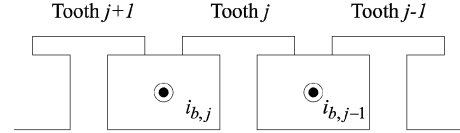


Fig. 2. Rotor geometry.

rotor to the stator, in a machine with a continuously distributed winding of turns density $N(\phi_s)$, the winding function satisfies

$$\frac{dW(\phi_s)}{d\phi_s} = -N(\phi_s). \quad (7)$$

The number of spans is determined by integrating the turn density. The constant of integration is arbitrary since, by Gauss’s law, the integral of the flux density around the air gap is zero, but is normally determined such that the average value of the winding function as ϕ_s varies from 0 to 2π is zero—a practice that results in MMF associated with a given winding to be equal to the winding function for that winding times the winding current.

In a machine in which the windings are lumped into discrete positions (slots), the number of spans is a discrete variable calculated in accordance with

$$W_{i+1} = W_i - N_i \quad (8)$$

where N_i and W_i are the turns in slot i and span between slot i and slot $i + 1$, respectively. In (8), W_1 is selected so that

$$\sum_{i=1}^{N_{ss}} W_i = 0. \quad (9)$$

In the three-phase system discussed herein, the span vector $\mathbf{W}_{abc,i}$ is defined as

$$\mathbf{W}_{abc,i} = [W_{a,i} \ W_{b,i} \ W_{c,i}]^T \quad (10)$$

and is governed by

$$\mathbf{W}_{abc,i+1} = \mathbf{W}_{abc,i} - \mathbf{N}_{abc,i} \quad (11)$$

subject to the constraint that

$$\sum_{i=1}^{N_{ss}} \mathbf{W}_{abc,i} = [0 \ 0 \ 0]^T. \quad (12)$$

B. Rotor Definitions

The rotor structure is depicted in Fig. 2. Therein, open rotor bars are shown but this need not be the case. The squirrel cage rotor consists of N_{rs} rotor bars separated by N_{rs} rotor teeth. The bars and teeth are indexed $1, \dots, N_{rs}$. The current flowing in rotor bar j is denoted $i_{b,j}$.

The electrical connection of the bars is depicted in Fig. 3. Therein $r_{b,j}$, $r_{fe,j}$, and $r_{be,j}$ denote the resistance of the j th rotor bar, the resistance of the segment of the front end ring that connects bar j to bar $j + 1$, and the resistance of the segment of the back-end ring that connects bar j to bar $j + 1$, respectively. The provision to allow these to vary in a bar-by-bar fashion is included in order to accommodate damaged rotor conditions.

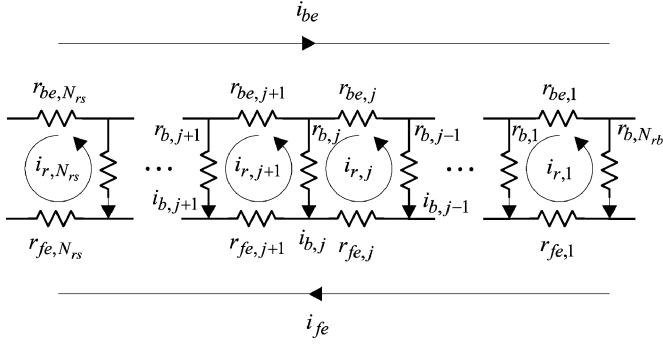


Fig. 3. Electrical rotor connections.

The loop current flowing around tooth j (with a sign convention such that positive current will cause a positive flux outward in the radial direction) is denoted $i_{r,j}$. The loop currents are related to the bar currents by

$$i_{b,j} = i_{r,j} - i_{r,j+1}. \quad (13)$$

Finally, the loop current around the front and back-end rings are denoted i_{fe} and i_{be} , respectively, and are defined with a direction such that the flux associated with these loops is outward in the axial direction. Although the set of loop currents $[i_{r,1}, \dots, i_{r,N_{rs}}, i_{fe}, i_{be}]$ are independent, physically, the description of the corresponding branch currents through the bars in segments is not unique, and so one of these may be assigned arbitrarily. In order to simplify the analysis to follow, the current i_{be} is set to zero.

The flux linking the path of loop current $i_{r,j}$ will be denoted $\lambda_{r,j}$. The area of this flux is defined to be from the center of bar $j-1$ to the center of bar j , and extend the length of the stack of the machine. By Ohm's and Faraday's laws, the loop currents are related to the flux linkages by

$$0 = r_{b,j}(i_{r,j} - i_{r,j+1}) + r_{b,j-1}(i_{r,j} - i_{r,j-1}) + r_{be,j}i_{r,j} + r_{fe,j}(i_{r,j} - i_{fe}) + p\lambda_{r,j} \quad (14)$$

where i_{be} has been taken to be zero. The flux linking the surface enclosed by the path of i_{be} and i_{fe} will be denoted λ_{be} and λ_{fe} , respectively. From Fig. 3, and again taking i_{be} to be zero

$$0 = -\sum_{j=1}^{N_{rs}} r_{be,j}i_{r,j} + p\lambda_{be} \quad (15)$$

$$0 = \sum_{j=1}^{N_{rs}} r_{fe,j}(i_{fe} - i_{r,j}) + p\lambda_{fe}. \quad (16)$$

By Gauss' law, the flux linkages $\lambda_{r,j}$, λ_{be} , and λ_{fe} are not independent. Instead, they must satisfy

$$\sum_{j=1}^{N_{rb}} \lambda_{r,j} + \lambda_{be} + \lambda_{fe} = 0. \quad (17)$$

In (17), note that each flux linkage can be interpreted as a simple flux since each flux linkage is associated with a single turn.

Finally, as a matter of definition, the rotor quantities will be represented in vector form as

$$\mathbf{f}_r = [f_1, \dots, f_{N_{rs}}]^T. \quad (18)$$

C. Transformation of Stator Variables

Instead of analyzing the machine in terms of abc phase variables, it is convenient to utilize $qd0$ variables. The reasons for this are twofold. First, it leads to simplification of the analysis for the wye-connected case whereupon the zero sequence components can be neglected (automatically eliminating cut-sets associated with the fact that the sum of the currents is zero). Second, it leads to a simplification in calculation of the leakage inductance. In particular, in terms of abc variables there can be mutual leakage inductance between the stator windings. In terms of $qd0$ variables, however, the mutual leakage inductance between windings, can, in general, be neglected.

The transformation between $qd0$ variables and abc variables may readily be expressed in the form

$$\mathbf{f}_{qd0} = \mathbf{K}_s \mathbf{f}_{abc} \quad (19)$$

where $qd0$ variables are of the form

$$\mathbf{f}_{qd0} = [f_q \quad f_d \quad f_0]^T \quad (20)$$

and the transformation \mathbf{K}_s is taken to be

$$\mathbf{K}_s = \sqrt{\frac{2}{3}} \begin{bmatrix} \cos \theta & \cos(\theta - 2\pi/3) & \cos(\theta + 2\pi/3) \\ \sin \theta & \sin(\theta - 2\pi/3) & \sin(\theta + 2\pi/3) \\ 1/\sqrt{2} & 1/\sqrt{2} & 1/\sqrt{2} \end{bmatrix}. \quad (21)$$

Note that this is not the standard qd -transformation as set forth in, for example, [11]. This transformation was first proposed in [12], though not in the context of magnetic circuit modeling.

D. Model Integration

The fundamental property of a time-domain model is the ability to calculate the output variables and time derivatives of the state variables based on the input variables and the state variables. The inputs to the electrical model will be the stator voltages \mathbf{v}_{abc} and the electrical rotor position θ_r . The outputs will be the stator currents \mathbf{i}_{abc} and electromagnetic torque, T_e . The state variables will be the stator flux linkage vector (expressed in terms of $qd0$ variables) λ_{qd0} , the rotor flux linkage vector λ_r , and the front-end rotor flux λ_{fe} [λ_{be} is not used as a state variable because it is algebraically related to λ_r and λ_{be} by (17)].

The algorithm to do this is, in theory, straightforward. In particular, given the rotor position and stator and rotor flux linkages, the currents \mathbf{i}_{qd0} , \mathbf{i}_r , and i_{fe} can be found. Once this is accomplished, the time derivatives of the stator flux linkages may be expressed

$$p\lambda_{qd0} = \mathbf{v}_{qd0} - r_s \mathbf{i}_{qd0} \quad (22)$$

where \mathbf{v}_{qd0} is calculated using (19) and the time derivatives of the rotor flux linkages are given by

$$p\lambda_{r,j} = -r_{b,j}(i_{r,j} - i_{r,j+1}) - r_{be,j}(i_{r,j} - i_{be})$$

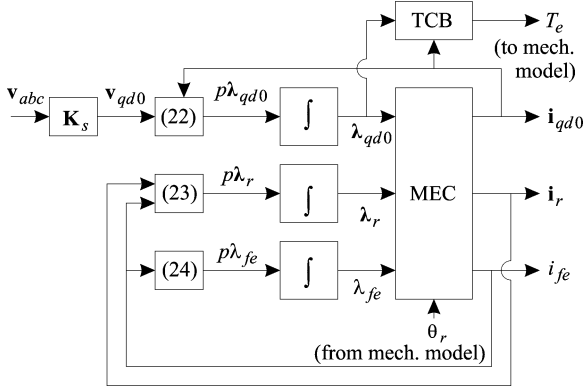


Fig. 4. Structure of electrical model.

$$-r_{b,j-1}(i_{r,j} - i_{r,j-1}) - r_{fe,j}(i_{r,j} - i_{fe}) \quad (23)$$

$$p\lambda_{fe} = - \sum_{j=1}^{N_{rs}} r_{fe,j}(i_{fe} - i_{r,j}) \quad (24)$$

where (22) was obtained by applying the transformation (21) to (5), and (23) and (24) were derived by straightforward manipulation of (15) and (16), respectively.

Fig. 4 illustrates the structure of the electrical model. Therein, T_e denotes the electromagnetic torque, which will be an algebraic function of electrical states and an output to the mechanical model; it is calculated in a torque calculation block (TCB) described in Section IV-D. The angle θ_r is the electrical rotor position that is a state of the mechanical model. The remainder of this paper is devoted to the MEC block, wherein the stator and rotor currents, i_{qd0} , i_r , and i_{fe} are calculated from the stator flux linkage vector (expressed in terms of $qd0$ variables) λ_{qd0} , the rotor flux linkage vector λ_r , the rotor end flux linkage λ_{fe} , and the rotor position θ_r . Note that the current i_{be} does not appear in Fig. 4 since, as previously discussed, it can be set to zero without loss of generality.

IV. MEC MODELING

The approach used to calculate the currents from the flux linkages and position will be MEC modeling. The stator and rotor equivalent circuits are depicted in Figs. 5 and 6, respectively. These figures also serve to define the node potentials and principal permeances associated with the model. As can be seen in Fig. 6, all potentials are referenced to the center of the rotor.

Leakage permeances, which would appear in parallel with the MMF sources in Figs. 5 and 6, are not shown in these diagrams; they will be considered when formulating the flux linkage equations. The stator MMF source may be represented as being either in the yoke or the tooth; it is placed in the yoke herein so that its value ($i_{s,i}$) directly corresponds to the current in the corresponding slot. From Fig. 5, and noting that the slot current in the i th stator slot is given by

$$i_{s,i} = \mathbf{N}_{qd0,i}^T \mathbf{i}_{qd0} \quad (25)$$

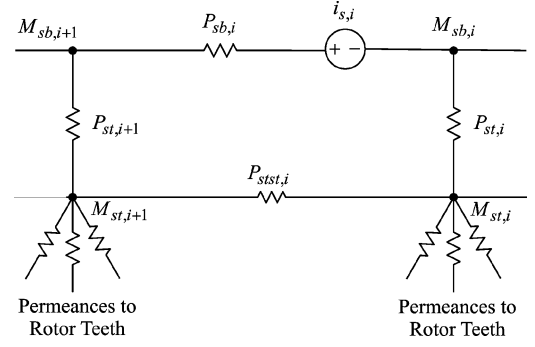


Fig. 5. Stator MEC.

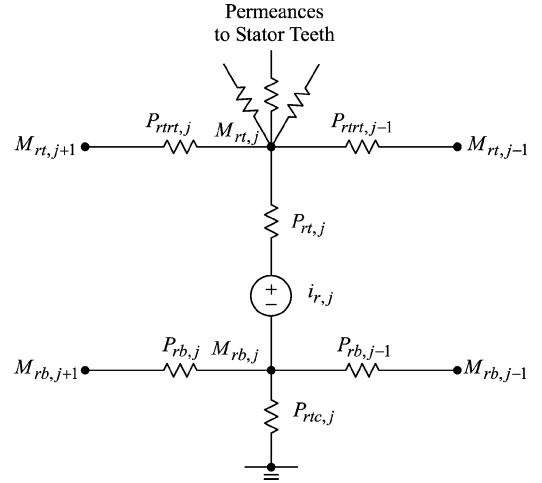


Fig. 6. Rotor MEC.

where $N_{qd0,i}$ is related to $N_{abc,i}$ by (18), the stator nodal equations may be readily expressed as

$$\begin{aligned} &P_{st,i}(M_{sb,i} - M_{st,i}) \\ &+ P_{sb,i-1}(M_{sb,i} - M_{sb,i-1} - \mathbf{N}_{qd0,i-1}^T \mathbf{i}_{qd0}) \\ &+ P_{sb,i}(M_{sb,i} - M_{sb,i+1} + \mathbf{N}_{qd0,i}^T \mathbf{i}_{qd0}) = 0 \end{aligned} \quad (26)$$

and

$$\begin{aligned} &P_{st,i}(M_{st,i} - M_{sb,i}) + P_{stst,i-1}(M_{st,i} - M_{st,i-1}) \\ &+ P_{stst,i}(M_{st,i} - M_{st,i+1}) \\ &+ \sum_{j=1}^{N_{rt}} P_{rtst,i,j}(M_{st,i} - M_{rt,j}) = 0. \end{aligned} \quad (27)$$

Equations (26) and (27) may also be written as

$$\mathbf{A}_{sb-sb} \mathbf{M}_{sb} + \mathbf{A}_{sb-st} \mathbf{M}_{st} + \mathbf{A}_{sb-si} \mathbf{i}_{qd0} = \mathbf{0} \quad (28)$$

$$\mathbf{A}_{st-sb} \mathbf{M}_{sb} + \mathbf{A}_{st-st} \mathbf{M}_{st} + \mathbf{A}_{st-rt} \mathbf{M}_{rt} = \mathbf{0}. \quad (29)$$

Consideration of Fig. 6 leads to the rotor nodal equations

$$\begin{aligned} &P_{rt,j}(M_{rt,j} - M_{rb,j} - i_{r,j}) \\ &+ P_{rtrt,j-1}(M_{rt,j} - M_{rt,j-1}) \end{aligned}$$

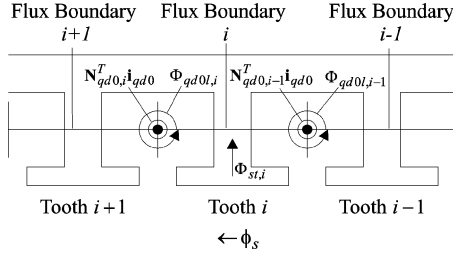


Fig. 7. Stator flux linkage flux paths.

$$+ P_{rt,rt,j}(M_{rt,j} - M_{rt,j+1}) + \sum_{i=1}^{N_{ss}} P_{rt,st,i,j}(M_{rt,i} - M_{st,j}) = 0 \quad (30)$$

$$P_{rt,j}(M_{rb,j} - M_{rt,j} + i_{r,j}) + P_{rb,j-1}(M_{rb,j} - M_{rb,j-1}) + P_{rb,j}(M_{rb,j} - M_{rb,j+1}) + P_{rtc,j}M_{rb,j} = 0 \quad (31)$$

which may also be expressed in matrix-vector form as

$$\mathbf{A}_{rt-st}\mathbf{M}_{st} + \mathbf{A}_{rt-rt}\mathbf{M}_{rt} + \mathbf{A}_{rt-sb}\mathbf{M}_{rb} + \mathbf{A}_{rt-ri}\mathbf{i}_r = \mathbf{0} \quad (32)$$

$$\mathbf{A}_{rb-rt}\mathbf{M}_{rt} + \mathbf{A}_{rb-rb}\mathbf{M}_{rb} + \mathbf{A}_{rb-ri}\mathbf{i}_r = \mathbf{0} \quad (33)$$

where the submatrices in (32) and (33) may be established by comparison to (30) and (31).

A. Stator Flux Linkage Equations

Fig. 7 depicts the flux paths used in the derivation of the stator flux linkage equations. Therein, note that all radial flux entering sector i links the q -, d -, and 0 -axis circuits $W_{q,i}$, $W_{d,i}$, and $W_{0,i}$ times, respectively. The flux entering this sector has two sources. First, there is the flux that enters the stator tooth. From Fig. 5, this flux may be expressed

$$\Phi_{st,i} = P_{st,i}(M_{st,i} - M_{sb,i}). \quad (34)$$

This component of the flux includes magnetizing flux as components of the leakage flux that travel through the MEC.

Adding up the number of times each of these flux components link each of the axis windings yields

$$\lambda_{qd0} = \sum_{i=1}^{N_{ss}} \mathbf{W}_{qd0,i} \circ \Phi_{st,i} [1 \ 1 \ 1]^T + \mathbf{L}_1 i_{qd0}. \quad (35)$$

In (35), \mathbf{L}_1 represents a leakage inductance matrix that takes into account the fact that there will be components of the flux linkage not included in the MEC. The calculation of \mathbf{L}_1 will be set forth in Section VI.

In matrix vector form (35) may be rewritten as

$$\mathbf{A}_{s\lambda-sb}\mathbf{M}_{sb} + \mathbf{A}_{s\lambda-st}\mathbf{M}_{st} + \mathbf{L}_1 \mathbf{i}_{qd0} = \lambda_{qd0}. \quad (36)$$

B. Rotor Flux Linkage Equations

The rotor end flux linkages are given by

$$\lambda_{fe} = \sum_{j=1}^{N_{rs}} P_{fe,j}(i_{fe} - i_{r,j}) \quad (37)$$

and

$$\lambda_{be} = - \sum_{j=1}^{N_{rs}} P_{be,j} i_{r,j} \quad (38)$$

wherein $P_{fe,j}$ and $P_{be,j}$ denote the permeances of the magnetic path around the front and back rotor end ring segments, respectively, and i_{be} is taken to be zero in accordance with the comments of Section III.

The flux linking each current loop may be expressed as

$$\lambda_{r,j} = P_{b,j}(i_{r,j} - i_{r,j+1}) + P_{b,j-1}(i_{r,j} - i_{r,j-1}) + P_{fe,j}(i_{r,j} - i_{fe}) + P_{be,j}i_{r,j} + \Phi_{mr,j} \quad (39)$$

where $P_{b,j}$ is the permeance of the magnetic path inside the j th bar and $\Phi_{mr,j}$ is the flux through the rotor tooth that may be expressed

$$\Phi_{mr,j} = P_{rt,j}(M_{rb,j} - M_{rt,j} + i_{r,j}). \quad (40)$$

Substitution of (37), (38), and (40) into (39) yields

$$\begin{aligned} \hat{\lambda}_{r,j} &= P_{rt,j}M_{rb,j} - P_{rt,j}M_{rt,j} - P_{b,j-1}i_{r,j-1} - P_{b,j}i_{r,j+1} \\ &\quad + (P_{b,j} + P_{b,j-1} + P_{fe,j} + P_{be,j} + P_{rt,j})i_{r,j} \\ &\quad - \frac{P_{fe,j}}{P_{\Sigma fe}} \sum_{k=1}^{N_{rs}} P_{fe,k} i_{r,k} \end{aligned} \quad (41)$$

where

$$\hat{\lambda}_{r,j} = \lambda_{r,j} + \frac{P_{fe,j}}{P_{\Sigma fe}} \lambda_{fe} \quad (42)$$

and

$$P_{\Sigma fe} = \sum_{j=1}^{N_{rs}} P_{fe,j}. \quad (43)$$

Equation (41) is readily formulated as

$$\mathbf{A}_{r\lambda-rt}\mathbf{M}_{rt} + \mathbf{A}_{r\lambda-rb}\mathbf{M}_{rb} + \mathbf{A}_{r\lambda-ri}\mathbf{i}_r = \hat{\lambda}_r^T \quad (44)$$

C. MEC Solution Algorithm

The relationships of (28), (29), (32), (33), (36), and (44) form a set of $2N_{ss} + 3N_{rs} + 3$ equations and the same number of unknowns. They may be expressed as

$$\mathbf{A}\mathbf{x} = \mathbf{b} \quad (45)$$

where \mathbf{A} , \mathbf{x} , and \mathbf{b} are partitioned matrices of the form

$$\mathbf{A} =$$

$$\begin{bmatrix} \mathbf{A}_{sb-sb} & \mathbf{A}_{sb-st} & 0 & 0 & \mathbf{A}_{sb-si} & 0 \\ \mathbf{A}_{st-sb} & \mathbf{A}_{st-st} & \mathbf{A}_{st-rt} & 0 & 0 & 0 \\ 0 & \mathbf{A}_{rt-st} & \mathbf{A}_{rt-rt} & \mathbf{A}_{rt-rb} & 0 & \mathbf{A}_{rt-ri} \\ 0 & 0 & \mathbf{A}_{rb-rt} & \mathbf{A}_{rb-rb} & 0 & \mathbf{A}_{rb-ri} \\ \mathbf{A}_{s\lambda-sb} & \mathbf{A}_{s\lambda-st} & 0 & 0 & \mathbf{L}_l & 0 \\ 0 & 0 & \mathbf{A}_{r\lambda-rt} & \mathbf{A}_{r\lambda-rb} & 0 & \mathbf{A}_{r\lambda-ri} \end{bmatrix}, \quad (46)$$

$$\mathbf{x} = [\mathbf{M}_{sb}^T \quad \mathbf{M}_{st}^T \quad \mathbf{M}_{rt}^T \quad \mathbf{M}_{rb}^T \quad \mathbf{i}_{qd0}^T \quad \mathbf{i}_r^T]^T \quad (47)$$

and

$$\mathbf{b} = \begin{bmatrix} 0 & 0 & 0 & 0 & \lambda_{qd0}^T & \hat{\lambda}_r^T \end{bmatrix}. \quad (48)$$

In this system of equations, each 0 represents a null matrix of appropriate dimensions, and subscripts “sb,” “st,” “rt,” “rb,” “si,” “ri,” “sλ,” and “rλ” denote association (either that this element came from that equation, or is multiplied by that variable) with the potential of stator base, potential of stator tooth, potential of rotor tooth, potential of rotor base, stator current, rotor current, stator flux linkage, and rotor flux linkage, respectively.

The system (45) is bilinear since many of the elements of \mathbf{A} are a function of permeabilities that are in turn a function of \mathbf{x} . The system can be solved using any nonlinear solution algorithm. For this work, a Gauss–Seidel iteration was used (starting from the previous solution). In particular, the algorithm proceeds as follows.

- 1) Calculate constant permeances and leakage inductances. This step is only conducted once at the beginning of a simulation. Expressions for permeances are given in Sections V and VI.
- 2) Based on the rotor position, calculate the stator to rotor permeances as discussed in Section V-C.
- 3) Based on node potentials and currents, calculate field intensity in each branch, and then the corresponding value of permeability. Then calculate permeances or iron estimate defined in Sections V-A and V-B.
- 4) Using the results of Steps 1–3 form system (45) and solve. If

$$\begin{aligned} |\mathbf{x}_{k_e} - \mathbf{x}_{k-1_e}| &< \varepsilon |\mathbf{x}_{k_e} + \mathbf{x}_{k-1_e}| \\ \forall e \in [1, \dots, N_{ss} + 2N_{rs} + 3] \end{aligned} \quad (49)$$

then convergence has been obtained and the algorithm proceeds to Step 5; otherwise the algorithm goes to Step 3. In (49), \mathbf{x}_k and \mathbf{x}_{k-1} denote present and previous estimate of \mathbf{x} and subscript ‘e’ denotes element index.

- 5) Note that the solution for \mathbf{x} includes currents \mathbf{i}_{qd0} and \mathbf{i}_r . The current i_{fe} may be found from (27) (after rearrangement). These currents are the output of the MEC.

D. Calculation of Torque

For this work, the torque was computed using the expression [11]

$$T_e = \frac{P}{2} (\lambda_d i_q - \lambda_q i_d) \quad (50)$$

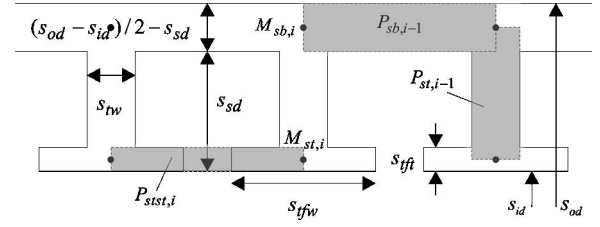


Fig. 8. Stator permeance geometry.

where P is the number of poles in the machine. The $3/2$ term usually present in (50) is eliminated by choice of reference frame. This expression will be shown to give acceptable results with regard to the average torque; the use of a more rigorous formulation is left for future work.

V. PERMEANCE CALCULATIONS

A. Stator Permeance Sections

The calculation of the stator permeances is dependent upon the exact details of the machine geometry. Since the object of this work is to establish a framework, the expressions for the stator magnetizing permeances set forth herein are relatively straightforward and based on the geometry shown in Fig. 8. This figure represents a simplification of the motor geometry in that it is approximated as rectangular. Therein s_{od} is the stator outside diameter, s_{id} is the stator inside diameter, s_{tw} is the stator tooth width, s_{tfw} is the stator tooth face width, s_{tft} is the stator tooth flange thickness, and s_{sd} is the stator slot depth. Using the mean path approximation yields

$$P_{st,i} = \frac{4\mu_{Fe}(\bullet)s_{tw}L}{s_{od} - s_{id} + 2s_{sd}} \quad (51)$$

$$P_{sb,i} = \frac{\mu_{Fe}(\bullet)N_{ss}(s_{od} - s_{id} - 2s_{sd})L}{\pi(s_{od} + s_{id} + 2s_{sd})} \quad (52)$$

$$P_{stst,i} = \frac{\mu_0 N_{ss} s_{tft} L}{\pi(s_{id} + s_{tft}) - N_{ss} s_{tfw}} \quad (53)$$

wherein $\mu_{Fe}(\bullet)$ is the permeability in the appropriate region of material. This will be discussed in Section VIII.

B. Rotor Permeance Sections

The assumed rotor geometry is depicted in Fig. 9. This is a hybrid figure in the sense that the lower part of the diagram depicts the rotor as round while the upper part of the diagram depicts a small segment of the outside of the rotor in developed diagram format.

Superimposed on Fig. 9 are the locations of the node potentials $M_{rt,j}$ and $M_{rb,j}$ as well as the region the flux is assumed to be flowing in for the purpose of calculating the permeances $P_{rt,j-1}$, $P_{rt,j-1}$, $P_{rb,j}$, and $P_{rt,j}$. Before calculating these values, it is necessary to assign a value to the depth of the rotor base nodes, r_{dbn} . The reluctance of the base of one tooth to the base of the adjacent tooth is

$$R = \frac{2r_{dbn}}{\mu_{Fe} L r_{tw}} + \frac{\pi(r_{od} - 2r_{sd} - 2r_{dbn})}{2\mu_{Fe} L r_{dbn} N_{rb}}. \quad (54)$$

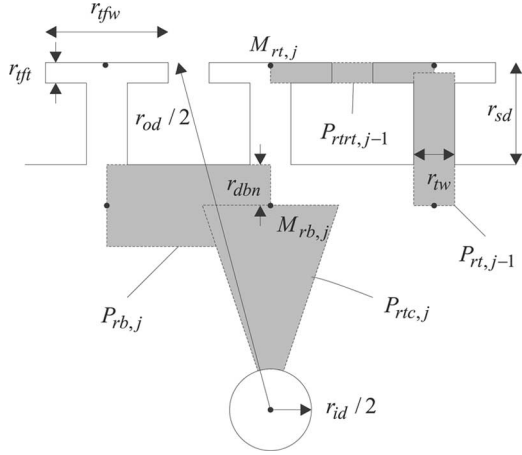


Fig. 9. Rotor permeance geometry.

Flux seeks the path of least reluctance; selecting the value of r_{dbn} that minimizes R yields

$$r_{dbn} = \frac{1}{2} \sqrt{\frac{\pi(r_{od} - 2r_{sd})r_{tw}}{N_{rb}}} \quad (55)$$

whereupon the rectangular approximation of the rotor tooth permeance is

$$P_{rt,j} = \frac{\mu_{Fe}(\bullet)Lr_{tw}}{r_{sd} + r_{dbn}} \quad (56)$$

and the rotor back-iron permeance is

$$P_{rb,j} = \frac{2\mu_{Fe,lin}Lr_{dbn}N_{rb}}{\pi(r_{od} - 2r_{sd} - 2r_{dbn})}. \quad (57)$$

The permeance from the base node to the center may be expressed

$$P_{rtc,j} = \frac{2\pi\mu_{Fe,lin}L}{N_{rb} \ln((r_{od} - 2r_{sd} - 2r_{dbn})/r_{id})}. \quad (58)$$

In (57) and (58), $\mu_{Fe,lin}$ is the permeability of the iron in the linear region since these regions do not saturate. Finally, the tooth tip to tooth tip permeance may be expressed

$$P_{rtrt,j} = \frac{\mu_0 N_{rs} r_{tft} L}{\pi(r_{id} - r_{tft}) - N_{rs} r_{tfw}}. \quad (59)$$

C. Stator–Rotor Permeances

The stator–rotor permeance is computed for every stator–rotor tooth combination and is denoted by $P_{rt,st:i,j}$. In order to compute the permeance between a particular stator–rotor tooth pair, the area of overlap between the teeth is computed whereupon

$$P_{rt,st:i,j} = \frac{a_{i,j} \times \mu_0}{g} \quad (60)$$

where g is the air gap length and $a_{i,j}$ is the area of overlap between the i th stator tooth and the j th rotor tooth. The area $a_{i,j}$ is calculated based on the machine geometry (taking skewing into account) and the instantaneous position of the rotor. The

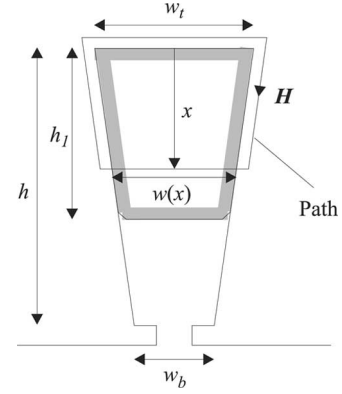


Fig. 10. Stator slot geometry.

details of the calculation of the area of tooth overlap are omitted but are straightforward to develop given the machine's geometry.

VI. LEAKAGE INDUCTANCE

A. Stator Leakage Calculation

The objective of this section is the calculation of the stator leakage matrix \mathbf{L}_1 . The first point that should be made is that the $\mathbf{L}_1 i_{qd0}$ component of the stator leakage flux represents the component of leakage flux that flows in a path not entirely contained in the MEC. The other components of the stator leakage flux that crossing from stator tooth tip to the adjacent stator tooth tip and the component that travels from the stator, across the air gap to the rotor, and again back to the stator without coupling the rotor current is computed as part of the MEC and is not included in this term. Thus, even though this term of the stator leakage flux will be treated as being linear, it does not mean that the overall stator leakage inductance is linear.

The premise of the method used to calculate \mathbf{L}_1 is the *a priori* assumption that this matrix is diagonal. This assumption is motivated by the formulation of the problem in terms of $qd0$ variables, wherein the windings are orthogonal, rather than abc variables, in which the windings are not orthogonal. Upon making this assumption, the calculation of each of the nonzero elements of \mathbf{L}_1 can be made independently.

Given that \mathbf{L}_1 is diagonal, it may be expressed as

$$\mathbf{L}_1 = \begin{bmatrix} L_{1q} & 0 & 0 \\ 0 & L_{1d} & 0 \\ 0 & 0 & L_{10} \end{bmatrix}. \quad (61)$$

In order to calculate \mathbf{L}_{1y} , where y may represent “ q ,” “ d ,” or “ 0 ,” consider Fig. 10, which shows the cross-sectional view of the i th trapezoidal-shaped stator slot. The width of the base and top of the slot are denoted by w_b and w_t , respectively and the height of the slot is denoted by h .

Winding y with $N_{y,i}$ turns is in the top portion of the slot as shown by the cross-hatch lines and has a height of h_1 . It should be observed that the other windings also occupy this same area. As stated previously, it is not necessary to include the effects of these windings since there will not be any net mutual leakage inductance through this path. However, it may strike the reader

as odd to assume that all the windings are located in the same physical space. To some extent, one may suppose that effects of this localization may somewhat average out. Further than this, though, it should be remembered that the windings being considered are the q , d , and 0 equivalent windings, not the a , b , and c . This has the result of effectively resulting in a more uniform distribution. For the purposes of analysis, the winding will be assumed to be perfectly uniform.

Given these assumptions, it can be shown that

$$L_{ly} = P_1 \sum_{i=1}^{N_{ss}} N_{y,i}^2 \quad (62)$$

where

$$P_1 = \frac{\mu_0 L \times K}{w_t h_1^2 (2K + h_1)^2} \left[K^4 \ln \left(\frac{K + h_1}{K} \right) - K^3 h_1 + \frac{K^2 h_1^2}{2} + K h_1^3 + \frac{h_1^4}{4} \right] + \frac{\mu_0 L h}{w_b - w_t} \ln \left(\frac{w_b h}{(w_b - w_t) h_1 + w_t h} \right) \quad (63)$$

In (63)

$$h_1 = \frac{w_t h}{w_t - w_b} - \sqrt{\frac{w_t^2 h^2}{(w_b - w_t)^2} + \left(\frac{w_b + w_t}{w_b - w_t} \right) h^2 s_{sf}} \quad (64)$$

where s_{sf} is the slot fill and

$$K = \frac{h w_t}{w_b - w_t} \quad (65)$$

$$w_t = \left(\frac{s_{id}}{2} + s_{sd} \right) \frac{2\pi}{N_{ss}} - s_{tw} \quad (66)$$

$$w_b = \left(\frac{s_{id}}{2} + s_{tft} \right) \frac{2\pi}{N_{ss}} - s_{tw} \quad (67)$$

$$h = s_{sd} - s_{tft}. \quad (68)$$

Observe that the stator end turn permeance has not been included, even though it could be in the proposed framework. This is because it is assumed that the included terms are dominant—an assumption that will be supported by the experimental results.

B. Rotor Leakage Calculation

The rotor leakage permeances $P_{b,j}$, $P_{fe,j}$, and $P_{be,j}$ are set forth in this section. The calculation of the rotor bar leakage permeance is based on Fig. 11. Therein, the trapezoidal area depicted represents the bar conductor within the slot. The width of the base and top of the slot are denoted w_b and w_t , respectively, and the height of the conductor area as h . The variable x denotes distance from the bottom of the slot and $w(x)$ denotes the width of the slot at a distance x from the bottom of the slot. Current is assumed to be flowing out of the conductor. In order to establish a formula for the leakage permeance, the field intensity will be calculated based on the path shown, and it will be assumed that along the air portion of this path the field intensity is uniform

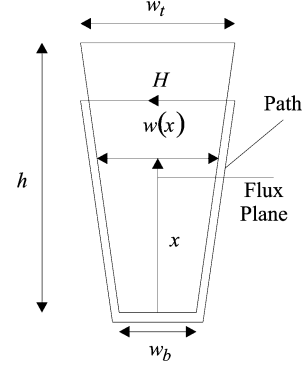


Fig. 11. Rotor bar leakage permeance.

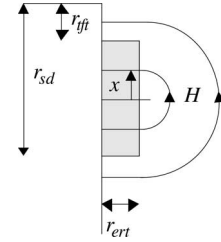


Fig. 12. End-bar leakage permeance.

and has a value $H(x)$ and everywhere else along the path is small enough to be neglected.

In order to calculate the leakage permeance $P_{b,j}$, note that the amount of this component of the leakage flux shown, which will cross the flux plane through the tooth, is the same as the flux passing the midline of the stator slot starting at the height of the flux plane and stopping at the top of the conductor (an additional component of leakage flux will flow from tooth to tooth across the tooth-to-tooth permeance, but this component has already been incorporated through the permeance $P_{rtrt,j}$). Based on these assumptions, it can be shown that

$$P_b = \frac{\mu_0 L h}{w_b + w_t} \left[\frac{3}{8} + \frac{w_b}{(w_t - w_b)^2} \left(\frac{w_t - w_b}{2} + w_b \ln \left(\frac{w_b + w_t}{2w_t} \right) \right) \right] \quad (69)$$

The basis for the calculation of the end-bar leakage permeances is depicted in Fig. 12. Therein the shaded area depicts a cross-sectional view of the end-bar conductor, with the machine itself folded into a developed diagram. Assuming the field intensity is only a function of x at its endpoint and follows the path shown, and that the field intensity in the rotor is zero

$$P_{fe,j} = P_{re,j} = \frac{\mu_0 L_{seg}}{\pi} \left[1 + \frac{4r_{ert}}{\pi h_1} \ln \left(\frac{4r_{ert}}{4r_{ert} + \pi h_1} \right) + \ln \left(\frac{4r_{ert} + \pi h_2}{4r_{ert} + \pi h_1} \right) \right] \quad (70)$$

where

$$h_1 = r_{sd} - r_{tft} \quad (71)$$

$$h_2 = r_{sd} + r_{tft} \quad (72)$$

and

$$L_{seg} = \frac{\pi}{N_{rs}}(r_{od} - r_{tft} - r_{sd}). \quad (73)$$

VII. RESISTANCE CALCULATIONS

Herein, an expression for the stator winding resistance is not given since it is normally straightforward to derive as a function of configuration. The rotor bar resistance, assuming no damage, may be readily expressed as

$$r_{b,j} = \frac{LN_{rs}\rho_{rc}}{(\pi(r_{od} - r_{tft} - r_{sd})) - r_{tw}N_{rs}}(r_{sd} - r_{tft}) \quad (74)$$

where ρ_{rc} denotes the resistivity of the rotor conductor material (typically aluminum or copper). Assuming that the end ring has the same radial dimension as the bar and a thickness r_{ert} , the end ring resistances may be expressed as

$$r_{fe,j} = r_{be,j} = \frac{\pi(r_{od} - r_{tft} - r_{sd})\rho_{rc}}{N_{rs}(r_{sd} - r_{tft})r_{ert}}. \quad (75)$$

VIII. MATERIAL CHARACTERISTICS

The permeability of the steel, μ_{Fe} , is computed as a function of the magnetic field intensity H in accordance with

$$\mu_{fe}(H) = \begin{cases} \frac{K_2 \ln(K_1|H|+1)}{K_1 K_2} & H \neq 0 \\ K_1 K_2 & H = 0 \end{cases} \quad (76)$$

where

$$H = \frac{\Delta M}{l} \quad (77)$$

and where ΔM is the magnetic potential across the iron section and l is the length of the iron section. A variety of alternatives to (76) and (77) exist. The only requirement is that the expression returns the permeability given the magnetic field intensity.

IX. EXPERIMENTAL RESULTS

Several studies were conducted to evaluate the performance of the MEC model. The parameters of the wye-connected, 230 V 1-l rms, 60 Hz, 5-hp test machine are listed in Table I, and the winding distribution is set forth in Table II. The apparatus for the laboratory tests was a Magtrol HD-815 dynamometer operating in constant speed mode. For each of the studies, the test motor was line fed from a 240-V three-phase source. In order to remove power quality issues from the simulation, the measured voltage waveforms were used as inputs to the simulation.

In conducting the studies, it was determined that the estimate of the rotor resistance based strictly on the resistivity of aluminum at 20 °C and the expressions (64)–(66) were low by approximately 27%. This can be explained by several factors, including porosity and impurities in the aluminum, skin effect, neglecting skewing when deriving (64) and (65), and temperature rise during startup. To correct this, the expressions for rotor

TABLE I
MACHINE PARAMETERS

N_{ss}	36	s_{ft}	0.2 mm	r_{ert}	11.0 mm
N_{rs}	28	r_{id}	35.0 mm	L	120 mm
s_{id}	104 mm	r_{od}	103 mm	P	4
s_{od}	170 mm	r_{sd}	19.1 mm	s_{sf}	432 mm
s_{sd}	17.1 mm	r_{tw}	5.61 mm	r_s	406 mΩ
s_{tw}	4.65 mm	r_{fw}	10.6 mm	$r_{r,mult}$	1.27
s_{fw}	6.48 mm	r_{ft}	0.5 mm	K_1	0.761 m/A
n	16.5	r_{sf}	27.8 mm	K_2	0.241 T

TABLE II
Turns Distribution

slot	1,	2,	3,	4,	5,	6,	7,	8,	9,
phase	19	20	21	22	23	24	25	26	27
a	n	n	n	0	0	0	0	0	0
b	0	0	0	0	0	0	n	n	n
c	0	0	0	-n	-n	-n	0	0	0

slot	10,	11,	12,	13,	14,	15,	16,	17,	18,
phase	28	29	30	31	32	33	34	35	36
a	-n	-n	-n	0	0	0	0	0	0
b	0	0	0	0	0	0	-n	-n	-n
c	0	0	0	n	n	n	0	0	0

resistance (64) and (65) were multiplied by the factor $r_{r,mult}$ in all of the studies.

Five studies were used to test the model; Study 1: balanced (source voltage) cold no load; Study 2: balanced cold full load; Study 3: balanced hot full load; Study 4: unbalanced cold full load; Study 5: balanced cold full load with broken rotor end ring. In the “cold” studies, the machine was at room temperature (20 °C), started, and the data taken as quickly as possible (though clearly the start-up transient would increase the rotor conductor temperature). For the “hot” study, the machine was allowed to run under load for approximately 1 h. The stator and rotor resistances used in the simulation were increased 25.7% and 15.6% from the cold values, respectively, to approximate the increase in resistance with temperature. This was based on the temperature coefficient of copper and aluminum, and assuming a 100 °C temperature rise. For the unbalanced study, a 2-Ω resistance was placed in series with the a -phase. An overview of the results from each study is shown in Table III. As can be seen, the MEC approach provides a reasonable estimate of machine performance. The no-load studies are at 1799 r/min due to the frictional and windage losses.

Fig. 13 illustrates the predicted and measured a -phase current waveforms, as well as the magnitude of the discrete Fourier transform (DFT) of the a -phase current waveforms for Study 1 (balanced cold no load). This DFT, as well as those for the remainder of the studies, was based on a 0.3-s data window sampled at 10 μs. As can be seen, the simulation provides a reasonable estimate of the magnitude and waveshape of the no-load current and current spectrum. In general, the spectral features of the measured data are broader than those predicted, and include minor peaks not predicted by the MEC model. These discrepancies are not unexpected since small asymmetries that physically exist will tend to broaden the spectral features and add additional spectral components. This can be verified

TABLE III
TEST RESULT OVERVIEW

Study	Speed (RPM)	Torque (Nm)	Real Power (W)	Reactive Power (Vars)	Power Factor	Power Out (W)	Power Loss (W)
1 sim	1799	0.572	146.8	2550	0.058	99.3	47.5
1 meas	1799	0.766	199.6	2609	0.076	144.3	55.3
2 sim	1750	24.90	4939	3057	0.850	4564	375.8
2 meas	1750	24.90	4966	3426	0.823	4563	402.7
3 sim	1750	21.76	4349	2890	0.833	3987	360.7
3 meas	1750	20.92	4145	3117	0.799	3835	310.2
4 sim	1760	18.56	3688	2493	0.828	3420	267.3
4 meas	1760	18.04	3609	2676	0.803	3324	284.9
5 sim	1750	23.69	4695	3117	0.833	4342	353.4
5 meas	1750	23.55	4708	3368	0.813	4316	391.3

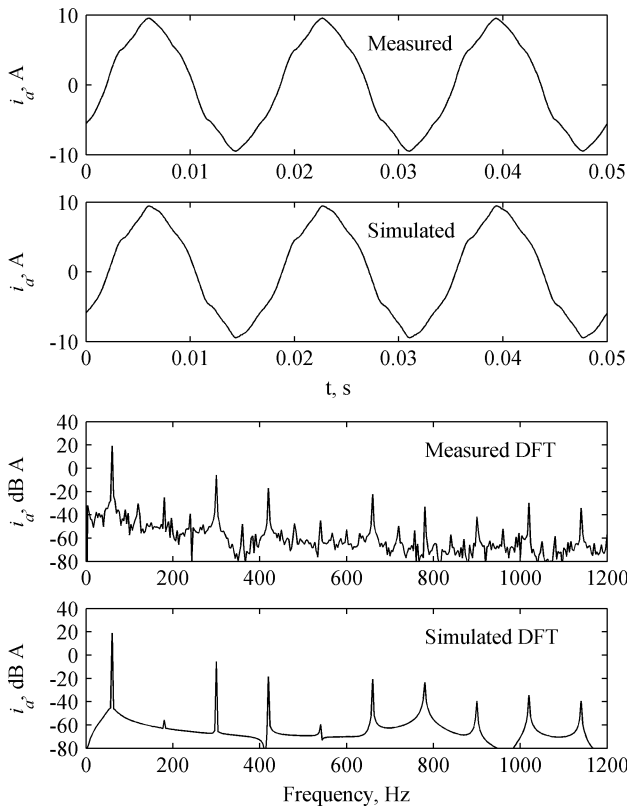


Fig. 13. Study 1 (balanced cold no load) results.

by incorporating asymmetries in the MEC model as will be discussed in Study 5.

Fig. 14 depicts Study 2 (balanced cold full load) results. Herein, it can be seen that while the estimate of the current waveform shape is reasonable, some spatial harmonics are somewhat overestimated, most likely due to the method of computing the stator tooth-rotor tooth permeance.

The DFT of the simulated performance in Study 2 contains features not seen in Study 1 due to the movement of the rotor teeth/bars relative to the stator MMF. The same effect can also be seen by comparing the measured DFTs, though in this case the effect is more subtle because of spectral features caused by bar-by-bar asymmetries.

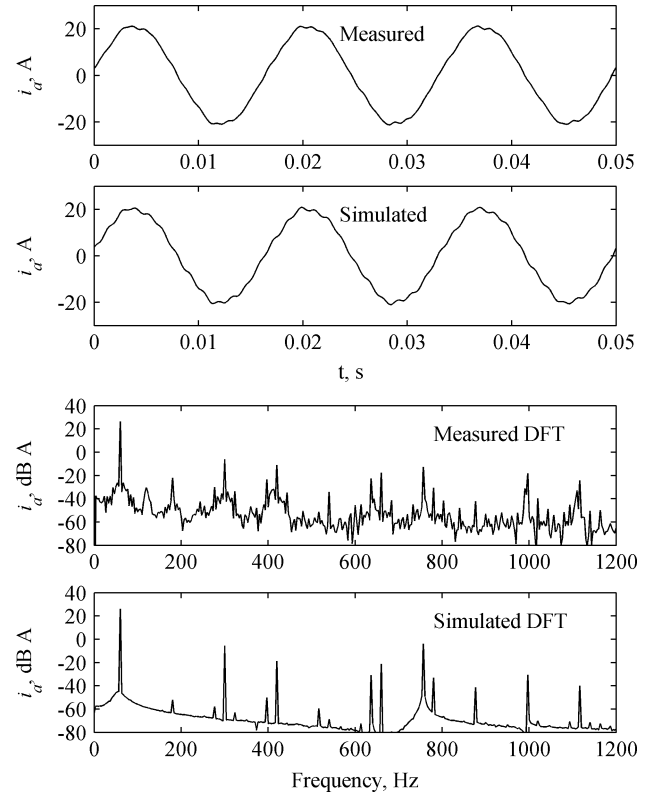


Fig. 14. Study 2 (balanced cold full load) results.

The simulated and measured time-domain waveforms and frequency spectrums for Study 3 (balanced hot full load) are shown in Fig. 15. The results are generally similar to those in Study 2 (Fig. 14).

The results of Study 4 (unbalanced cold full load) appear in Fig. 16. The simulated results are again in reasonable agreement with measurements. In this case, the number of low-level spectral features is reduced from the other loaded studies (both predicted and measured). This may be associated with increased damping because of the added a -phase resistance.

Finally Fig. 17 illustrates the performance for Study 5 (balanced cold full load with broken end ring). A feature of particular interest in this study is the broadening of the spectral features in the simulated DFT. This is suggestive that one reason that the measured DFT spectrum has consistently broader features than the measured spectrums could be bar-by-bar and end-ring-segment by end-ring-segment variation in resistance due to variation in porosity.

From a computational perspective, for the wye-connected machine there are $2 + N_{rs}$ state variables (flux linkages) and the number of unknowns in the MEC model (45) is $2N_{ss} + 3N_{rs} + 3$. Thus, for the sample machine, there are 31 electrical states and the system of algebraic equations associated with the MEC portion of the model is 159. This is a fraction of the order of equations that would be required by a FEM-based model.

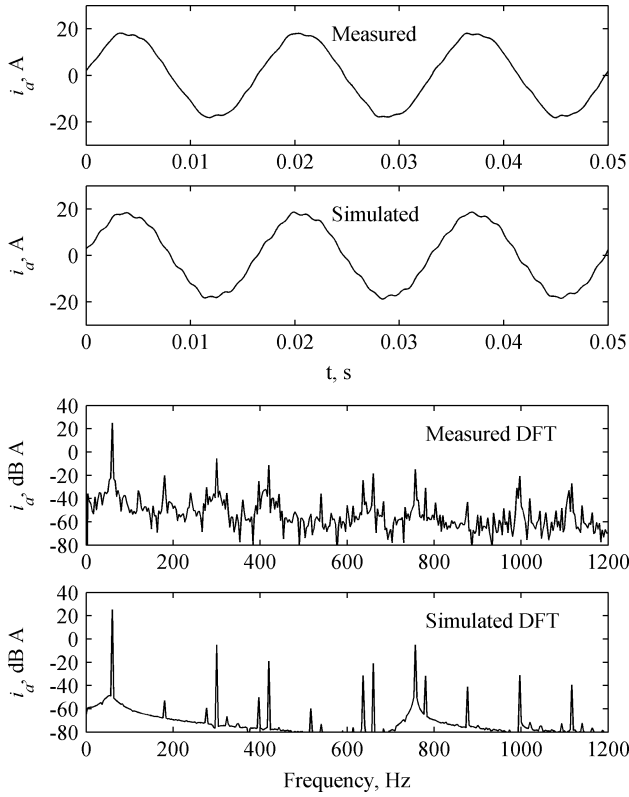


Fig. 15. Study 3 (balanced hot full load) results.

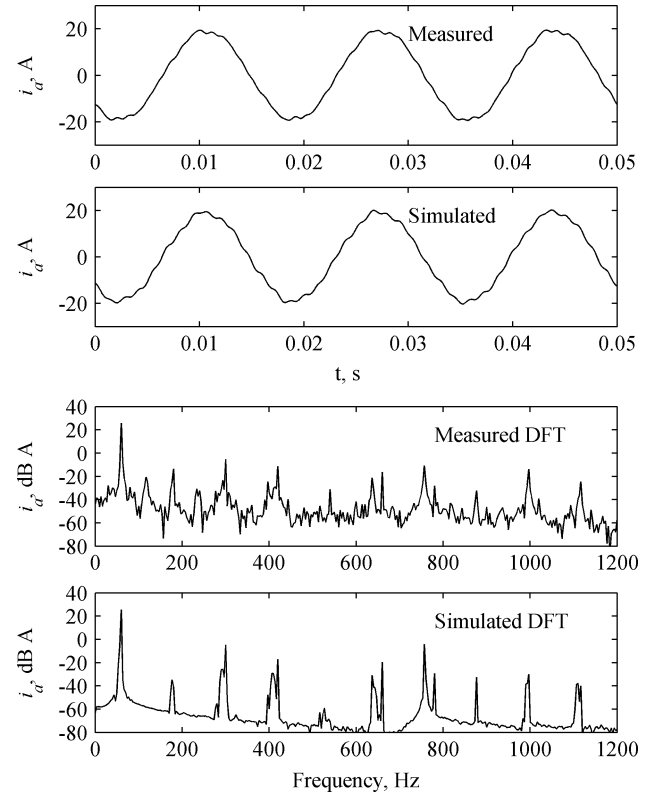


Fig. 17. Study 5 (broken end ring) results.

X. SUMMARY

An MEC representation of an induction machine is set forth and shown to be reasonably accurate in predicting machine performance over a range of operating points, including no-load conditions, loaded conditions, unbalanced excitation conditions, and broken end ring conditions. This model is notable in that all of the parameters are physical quantities—the dimensions of the motor, the lamination magnetic properties, and the winding configuration. The approach is an excellent compromise between the standard lumped-parameter models and time-stepped FEA in terms of computation time and accuracy.

REFERENCES

- [1] X. Lou, Y. Liao, H. A. Toliyat, A. El-Antably, and T. A. Lipo, "Multiple coupled circuit modeling of induction machines," *IEEE Trans. Ind. Appl.*, vol. 31, no. 2, pp. 311–318, Mar.–Apr. 1995.
- [2] H. A. Toliyat and T. A. Lipo, "Transient analysis of cage induction machines under stator, rotor bar, and end ring faults," *IEEE Trans. Energy Convers.*, vol. 10, no. 2, pp. 241–247, Jun. 1995.
- [3] V. Ostovic, "A method for evaluation of transient and steady state performance in saturated squirrel cage induction machines," *IEEE Trans. Energy Convers.*, vol. 1, no. 3, pp. 190–197, Sep. 1986.
- [4] —, "A simplified approach to magnetic equivalent-circuit modeling of induction machines," *IEEE Trans. Ind. Appl.*, vol. 24, no. 2, pp. 308–316, Mar.–Apr. 1988.
- [5] A. K. Wallace and A. Wright, "Novel simulation of cage windings based on mesh circuit model," *IEEE Trans. Power App. Syst.*, vol. PAS-93, pp. 377–382, Jan.–Feb. 1974.
- [6] C. Delforge and B. Lemaire-Semail, "Induction machine modeling using finite element and permeance network methods," *IEEE Trans. Magn.*, vol. 31, no. 3, pp. 2092–2095, May 1995.
- [7] G. R. Slemon, "An equivalent circuit approach to analysis of synchronous

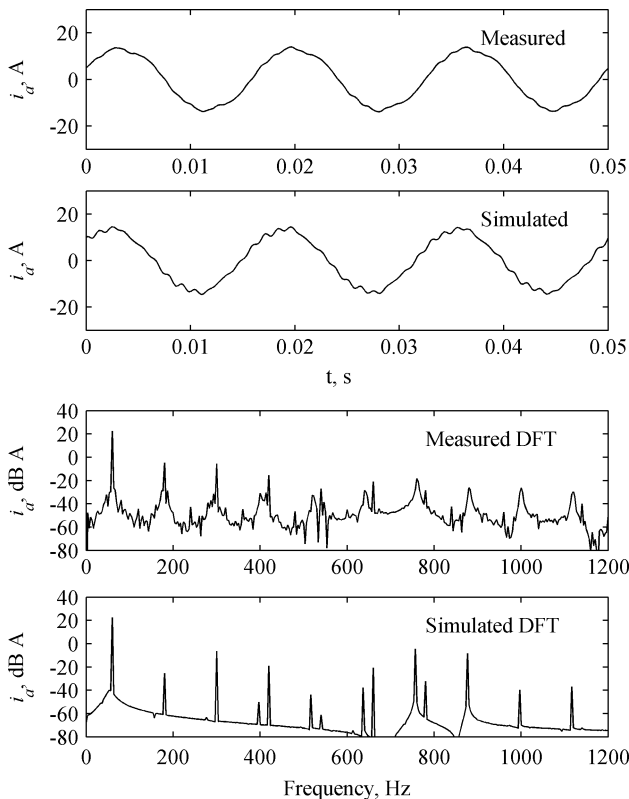


Fig. 16. Study 4 (unbalanced cold full load) results.

- machines with saliency and saturation," *IEEE Trans. Energy Convers.*, vol. 5, no. 3, pp. 538–545, Sep. 1990.
- [8] M. Moallem and G. E. Dawson, "An improved magnetic equivalent circuit method for prediction the characteristics of highly saturated electromagnetic devices," *IEEE Trans. Magn.*, vol. 34, no. 5, pt. 1, pp. 3632–3635, Sep. 1998.
- [9] A. R. Muñoz and T. A. Lipo, "Complex vector model of the squirrel-cage induction machine including instantaneous rotor bar currents," *IEEE Trans. Ind. Appl.*, vol. 35, no. 6, pp. 1332–1340, Nov.–Dec. 1999.
- [10] N. L. Schmitz and D. W. Novotny, *Introductory Electromechanics*. New York, Ronald, 1965.
- [11] P. C. Krause, O. Wasynczuk, and S. D. Sudhoff, *Analysis of Electric Machinery*. Piscataway, NJ: IEEE Press, 1996.
- [12] W. A. Lewis, "A basic analysis of synchronous machines—part I," *AIEE Trans.*, Part III. *Power App. Syst.*, vol. 77, no. 37, pp. 436–456, Aug. 1958.
- [13] R. Fiser, S. Ferkolj, and H. Solinc, "Steady state analysis of induction motor with broken rotor bars," in *Conf. Rec. 7th Int. Conf. Electr. Machines Drives*, 1995, pp. 42–46.
- Scott D. Sudhoff** (S'87–M'91–SM'01) received the B.S., M.S., and Ph.D. degrees, from Purdue University, West Lafayette, IN, in 1988, 1989, and 1991, respectively, all in electrical engineering.
- Currently, he is a Full Professor at the Department of Electrical and Computer Engineering, Purdue University.
- Brian T. Kuhn** (M'93) received the B.S. and M.S. degrees, from the University of Missouri-Rolla, Rolla, MO, in 1996 and 1997, respectively, both in electrical engineering.
- Currently, he is a Senior Engineer at SmartSpark Energy Systems, Champaign, IL.
- Keith A. Corzine** (S'92–M'97) received the B.S., M.S., and Ph.D. degrees, from the University of Missouri–Rolla, Rolla, MO, in 1992, 1994, and 1997, respectively, all in electrical engineering.
- Currently, he is an Associate Professor at the Department of Electrical and Computer Engineering, University of Missouri-Rolla.
- Brian T. Branecky** received the B.S. and M.S. degrees, from the Texas Tech University, Lubbock, TX, in 1986, and the University of Wisconsin-Milwaukee, Milwaukee, WI, in 1998, both in electrical engineering.
- Currently, he is a Principal Engineer at the A. O. Smith Corporate Technology Center, Milwaukee, WI.